

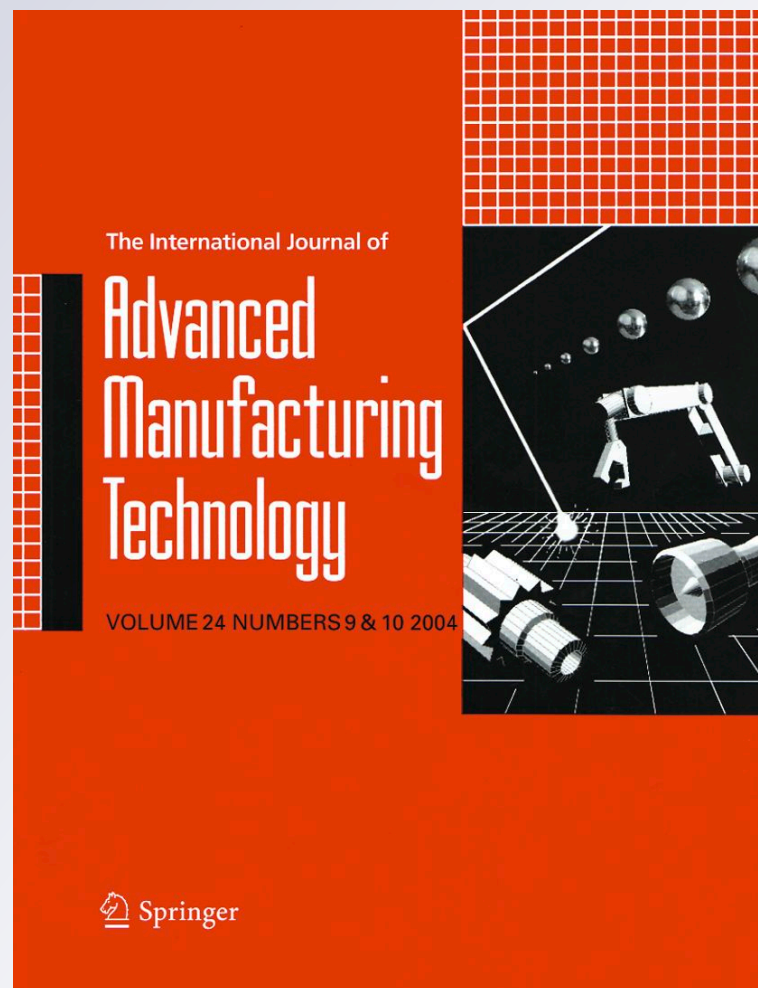
Modeling the powder compaction process using the finite element method and inverse optimization

*Meftah Hrairi, Hedi Chtourou, Augustin
Gakwaya & Michel Guillot*

**The International Journal
of Advanced Manufacturing
Technology**

ISSN 0268-3768
Volume 56
Combined 5-8

Int J Adv Manuf Technol (2011)
56:631-647
DOI 10.1007/s00170-011-3211-z



Your article is protected by copyright and all rights are held exclusively by Springer-Verlag London Limited. This e-offprint is for personal use only and shall not be self-archived in electronic repositories. If you wish to self-archive your work, please use the accepted author's version for posting to your own website or your institution's repository. You may further deposit the accepted author's version on a funder's repository at a funder's request, provided it is not made publicly available until 12 months after publication.

Modeling the powder compaction process using the finite element method and inverse optimization

Meftah Hrairi · Hedi Chtourou · Augustin Gakwaya · Michel Guillot

Received: 19 May 2009 / Accepted: 31 January 2011 / Published online: 26 February 2011
© Springer-Verlag London Limited 2011

Abstract This paper focuses on studying and adapting modeling techniques using the finite element method to simulate the rigid die compaction of metal powders. First, it presents the implementation of the cap constitutive model into ABAQUS FE software using the closest point projection algorithm. Then, an inverse modeling procedure was proposed to alleviate the problems raised by the interpretation of the experimental tests and to more accurately determine the material parameters. The objective function is formed, based on the discrepancy in density data between the numerical model prediction and the experiment. Minimization of the objective function with respect to the material parameters was performed using an in-house optimization software shell built on a modified Levenberg–Marquardt method. Thus, an integrated simulation module consisting of an inverse optimization method and a finite element method was developed for modeling the powder compaction process as a whole. The simulation and identification module developed was applied to simulate the compaction of some industrial parts. The results reveal that the maximum absolute error between densities is 2.3%. It corresponds to the precision of the experimental method.

Keywords Powder metallurgy · Compaction process · Finite element · Density · Inverse identification · Cap model · Abaqus · Material parameters · Iron powder

Nomenclature

I	Second order identity tensor
C	Fourth-order elasticity tensor
c_j	Constraint functions
$E(\rho)$	Young's modulus as a function of compact density
F_s	Function $F_s(I_1) = \alpha + \theta I_1 - \gamma \exp(-\beta I_1)$ in the shear failure surface equation
F_c	Function $F_c(I_1, \ \mathbf{s}\ , \kappa) = \sqrt{\ \mathbf{s}\ ^2 - \frac{[I_1 - L(\kappa)]^2}{R^2}}$ in the cap surface equation
f_1	Yield function of the tension surface
f_2	Yield function of the shear surface
f_3	Yield function of the cap surface
G	Shear modulus
g	First order derivatives of the weighted penalty functions with respect to the parameters
h	Second order derivatives of the weighted penalty functions with respect to the parameters
H^{ep}	Elastoplastic tangent moduli
I	Fourth-order identity tensor
I_1	First invariant of stress tensor
J_2	Second invariant of deviatoric stress tensor
J	Jacobian matrix of Φ
$K(\rho)$	Bulk modulus as a function of compact density
[K]	Stiffness matrix
m	Number of measured data
n	Number of parameters to be optimized
q	Number of constraints

M. Hrairi (✉)
Mechanical Engineering Department, International Islamic University Malaysia,
Gombak, Malaysia
e-mail: meftah@iiu.edu.my

H. Chtourou
Department of Technology, IPEIS, Sfax University,
Sfax, Tunisia

A. Gakwaya · M. Guillot
Mechanical Engineering Department, Laval University,
Quebec City, Canada

R	Aspect ratio of the cap surface
\mathbf{R}	Unbalanced load vector
\mathbf{r}	Residual vector
r_1, r_2, r_3	Material parameters describing the aspect ratio of the cap surface $R = r_1(\rho - r_2)^{r_3}$
\mathbf{s}	Deviatoric stress tensor
$\ \mathbf{s}\ = \sqrt{\mathbf{s} : \mathbf{s}}$	Norm of the deviatoric stress tensor
t	Time t
T	Material parameter (tension cutoff)
\mathbf{u}	Nodal displacement vector
W, D	Material parameters for hardening rule $\bar{\varepsilon}_v^p = W(1 - e^{-D \cdot X(\kappa)})$

Greek symbols

$\alpha, \beta, \gamma, \theta$	Material parameters for the shear failure $F_s(I_1) = \alpha - \gamma e^{(-\beta I_1)} + \theta I_1$
ε	Logarithmic strain
ρ	Relative density
ρ_0	Initial loose state relative density
τ	Kirchhoff stress
σ	Cauchy stress tensor
ζ	Weighted penalty function
ξ	Tolerance for convergence (specified positive number)
ω	Non-negative weight
$\delta \mathbf{p}^k$	Parameter correction
ψ	Helmholtz' free energy function
Φ	Cost function
Φ^*	Objective function
κ	Hardening parameter
λ_i	Plastic consistency parameters
μ	Levenberg-Marquardt parameter
$\Delta(\cdot)$	Increment of a quantity
$\partial(\cdot)$	Partial derivative of a quantity

Subscripts

0	index for initial value
1, 2, 3	indices for tension, shear and cap failure surfaces respectively
c	cap surface
g	geometric
l	linearization
j	index for the number of constraints $j=1, q$
m	material
$n, n+1$	indices for successive configurations
s	shear failure surface
v	volumetric

Superscripts

cal	calculated using finite element
e	elastic
exp	experimental
k	iteration
p	plastic

T	tangent
Trial	trial or elastic prediction

1 Introduction

Powder metallurgy (P/M) has become widely recognized as a robust process for producing high-quality parts for a variety of important applications. This success is due to the advantages the process offers over other metal forming technologies such as forging and metal casting; advantages in material utilization, shape complexity, near-net shape dimensional control, among others [1]. The P/M process can be broken down into three main manufacturing steps: mixing of the powder, compaction, and sintering. More than any other operation, it is the compaction, which is generally performed using a set of punches and dies, mounted onto a hydraulic or mechanical press that controls the practical application of powder metallurgy. The semi-finished product resulting from the compaction operation is a compact having a nearly final form but a very weak mechanical resistance sufficient only to ensure its transfer to the next step in the process: sintering.

The modeling of the compaction operation is used to optimize not only this step, but ulterior steps as well. In recent years, several types of constitutive models have been developed and applied in the analysis of the compaction of metal powders. Most of the proposed constitutive models belong to one of the following two classes: porous material models and granular material models. Porous material models are based on the classical von Mises model in which some modifications are introduced in order to account for the influence of the hydrostatic pressures on the yield criterion [2–4]. Since these models are a simple extension of classic elastoplasticity, they are consequently suitable to model the behavior of powders in high-density zones but unfortunately cannot be used to model the first stages of compression [5]. Also, this type of model would require a plasticity limit that is equivalent during compression and tension, which is not adequate for granular mediums. Granular material models, originally developed for rocks, soils, and other geological materials, are based on a multiple yield criterion approach and are naturally sensitive to hydrostatic stress and consider the cohesion and friction among the particles of granular matter. As a result of the suggestion that the low strength of powder compacts in shear and tensile stress field must be taken into account, models, such as the Drucker–Prager cap model [6], the Cam–Clay model [7], or the DiMaggio–Sandler model [8, 9] have been adapted from soil mechanics literature. These models are characterized by a yield criterion, a hardening function and a flow rule and they

differ by the functional form of the yield surface. In the Drucker–Prager cap model, the yield surface consists of an elliptical cap and a straight failure line. In the Cam–Clay model, both the failure surface and the cap are characterized by elliptic arcs with different eccentricity. In the DiMaggio–Sandler model the failure surface is given by an exponential function approaching the yield stress of the fully dense material at high pressures.

Because it captures important aspects of the physics of compaction, the DiMaggio–Sandler Cap model, on which the present work is based, is a frequently used continuum model for modeling the mechanical behavior of pharmaceutical powders during compaction [10–15] as well as in the simulation of metal powder compaction processes [16–20]. Indeed, this model reflects the yielding, frictional, and densification characteristics of powder along with strain and geometrical hardening which occur during the compaction process. However, the counterpart of this flexibility is the significant amount of experimental work required to properly calibrate the model parameters for a particular blend of powders [21–24]. Moreover, in these studies, the elastic moduli, as well as the cap aspect ratio, were assumed to be constant which was not suitable to describe the observed nonlinear unloading behavior of metal powders and to better represent ductile powder compaction behavior, respectively.

In this work, an enhanced Cap model for simulating the behavior of powders during rigid die compaction has been developed. This model allows for using variable elasticity as well as a density dependent cap aspect ratio. It was implemented into the finite element (FE) code ABAQUS as a user defined subroutine using a return mapping algorithm. The simulations were run by means of an integrated computer module that uses I-DEAS Master Series software for the geometrical definition of the problem, an in-house developed interface program for the determination of boundary conditions, ABAQUS software for the FE solution, and ABAQUS POST for the post-processing of the results. In addition, the sizeable amount of cap model parameters and experimental efforts required that these parameters to be determined, constitute a handicap for this family of models. From this, comes the necessity to create an alternate calibration procedure for the model, based on inverse problems, in order to determine the material parameters directly from production components. Thus, this work creates a complete module capable of using finite elements and inverse optimization to evaluate the density distribution resulting from the compaction process.

2 Cap plasticity model

To formulate the elastic-plastic constitutive equations in a large deformation framework, one should first choose an

appropriate work conjugate pair of stress and strain measurements [25, 26]. The logarithmic strains ϵ were chosen because they are the only measures that permit an additive decomposition of the strain in the large deformation range into elastic (ϵ^e) and plastic (ϵ^p) deformation tensors [25–27].

$$\epsilon = \epsilon^e + \epsilon^p \tag{1}$$

For the chosen strain measure, the conjugate stress measure is the Kirchhoff stress τ which can be approximated to the true Cauchy stress tensor σ in the case where elastic deformations are small compared to unity. The adopted stress–strain relationship corresponds to that of an isotropic hyperelastic solid where the elasticity parameters are density dependent:

$$\sigma = \mathbf{C}\epsilon^e = \mathbf{C}(\epsilon - \epsilon^p) \tag{2}$$

with

$$\mathbf{C} = \frac{\partial^2 \psi}{\partial \epsilon^2} = 2G(\rho)\mathbf{I} + (K(\rho) - 2/3G(\rho))\mathbf{1} \otimes \mathbf{1} \tag{3}$$

and where ψ is Helmholtz' free energy function, \mathbf{C} is the fourth-order elasticity tensor, \mathbf{I} and $\mathbf{1}$ are the fourth and second order identity tensors respectively, G and K are the shear and bulk moduli expressed as a function of the powder's relative density ρ .

Another main component of the constitutive model is the yield functions that separate the purely elastic behavior from the elastic plastic one. The yield surface of this elasto-plastic model has a moving cap, intersecting the hydrostatic loading line, whose position is a function of plastic volumetric strain, as shown in Fig. 1. The main features of the cap model include a failure surface and an elliptical yield cap which closes the open space between the failure surface and the hydrostatic axis. The yield cap expands in the stress space according to a specified hardening rule. The functional forms for these surfaces are

$$f_1 = I_1 - T = 0 \tag{4}$$

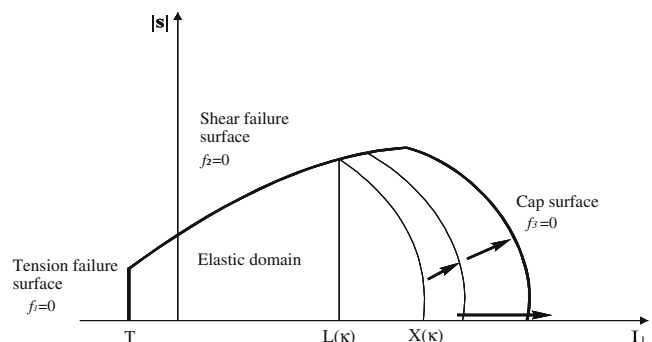


Fig. 1 Multi-surfaced Cap elastoplasticity model

$$f_2 = \|\mathbf{s}\| - F_s(I_1) = 0 \quad \text{where} \quad F_s(I_1) = \alpha + \theta I_1 - \gamma e^{-\beta I_1} \quad (5)$$

$$f_3 = F_c(I_1, \|\mathbf{s}\|, \kappa) - F_s(\kappa) = 0 \quad (6)$$

where $F_c(I_1, \|\mathbf{s}\|, \kappa) = \sqrt{\|\mathbf{s}\|^2 - \frac{[I_1 - L(\kappa)]^2}{R^2}}$

where I_1 is the first stress invariant, $\|\mathbf{s}\| = \sqrt{\mathbf{s} : \mathbf{s}} = \sqrt{2J_2}$ is the norm of the deviatoric stress tensor, κ is the hardening parameter, $\alpha, \beta, \gamma, \theta, R$ and T are material parameters, and

$$L(\kappa) = \begin{cases} \kappa & \text{if } \kappa > 0 \\ 0 & \text{if } \kappa \leq 0 \end{cases} \quad (7)$$

$$X(\kappa) = \kappa + R \cdot F_s(\kappa) \quad (8)$$

The tension and shear failure surfaces, f_1 and f_2 , respectively, represent the stress states that may cause fracture of the powder compact during its ejection or its compaction with very large local distortion. This is often caused by the different compaction ratios of powder columns in multilevel parts. The cap yield surface f_3 is an elliptical function, with R denoting the ratio of two elliptical cap's diameters. Traditionally, R was considered to be constant, which may be appropriate for non-cohesive and non-ductile materials such as geological materials. However, it is not realistic to model metal powder behavior using a cap having a constant axes ratio R . In this work, R has been implemented as an increasing function of the density. This allows for the proper modeling of the behavior similar to that of soils in the low pressure zone. But, when the pressures become important and the density becomes elevated, the plastic yielding becomes more susceptible to occur by a shear load than by a hydrostatic load. A flattened cap would be more representative of the compacted powder behavior at high densities.

For strain hardening in the compressive regime, an exponential function for the effective volumetric plastic strain $\bar{\epsilon}_v^p$ is used to govern the expansive and contractive behavior of the elliptical cap through the evolution of the state variable κ . This evolution is given by the hardening rule relating κ to the effective volumetric plastic strain $\bar{\epsilon}_v^p$ in a form suggested by the results of the classical hydrostatic pressing test

$$\bar{\epsilon}_v^p(X(\kappa)) = W \left[1 - e^{-D \cdot X(\kappa)} \right] \quad (9)$$

where, W and D are two material parameters and $\bar{\epsilon}_v^p$ is the effective plastic strain expressed in terms of the stress first

invariant $X(\kappa)$ and defined in a manner that prevents the cap strain from softening:

$$\bar{\epsilon}_v^p = \begin{cases} \epsilon_v^p & \text{if } \dot{\epsilon}_v^p > 0 \text{ or if } \kappa > 0 \text{ and } \kappa > I_1 \\ 0 & \text{otherwise} \end{cases} \quad (10)$$

The volumetric plastic strain ϵ_v^p is the trace of the plastic strain tensor ϵ^p . It is used to update the actual aggregate density ρ using the initial loose state density ρ_0 as follows:

$$\rho = \rho_0 e^{-\epsilon_v^p} \quad (11)$$

3 Computational algorithm of cap model

3.1 Finite element problem

The compaction process is assumed to be a quasi-static transformation with the final spatial distribution of density $\rho(\mathbf{x})$ as the driving unknown [28, 29]. Every material point undergoes finite strain deformation and elastoplastic transformations take place under the interaction of the powder medium and the tooling components. The corresponding nonlinear structural FE analysis involves integration of the differential elastoplastic equations in time and space. The time integration in the present context is due to the discretization of the loading history, while the spatial integration is normally performed via Gauss quadratures at the FE level and then assembled in terms of the mechanical degrees of freedom.

A nonlinear solver based on the Newton–Raphson method has been used. This choice is motivated by the presence of strong nonlinearities and the desired quadratic rate of convergence. The scheme used thus required the updating of the consistent tangent stiffness at each iteration and the use of the algorithmic tangent material operator [30]. Hence, at the end of each time step, the current stress state satisfies the equilibrium of the mechanical system with the external forces in a weak sense and complies with the full consistency of the elastoplastic material and frictional contact formulation.

In this nonlinear context where the principal unknown is the incremental nodal displacements vector $\{\Delta \mathbf{u}_{n+1}\}$ between configurations n and $n+1$, the discrete linearized FE approximation to be solved at each iteration k can be written as follows:

$$\begin{aligned} & [\mathbf{K}^T]^k \{\Delta \mathbf{u}\}^k \\ & = \left([\mathbf{K}_m^T] + [\mathbf{K}_g^T] + [\mathbf{K}_f^T] \right)^{k-1} \{\Delta \mathbf{u}_{n+1}\}^k \\ & = \{\Delta \mathbf{R}_{n+1}\}^k \end{aligned} \quad (12)$$

where $[K_m^T]$ is the material stiffness matrix, $[K_g^T]$ is the geometric stiffness matrix, $[K_l^T]$ is the contribution resulting from the linearization of contact forces and $\{\Delta R_{n+1}\}$ is the incremental unbalanced load vector. This equation is solved using a Newton–Raphson scheme following the algorithm summarized in Table 1.

3.2 Integration of the behavior law

The numerical integration procedure of the behavior model was completed according to the closest point projection algorithm. Calculation of the stresses is performed following an implicit scheme of prediction–correction and by using an operator split method [31]. First, the plastic evolution is assumed to be momentarily frozen and an elastic prediction is performed. If the plasticity criterion is violated by the prediction, then a plastic correction must be performed to take the yield that occurs into account. This algorithm is coded in Fortran 77 and implemented into the ABAQUS software using the User Material option UMAT. At each iteration, performed for a single load step corresponding to the passing of an equilibrium configuration C_n to following configuration C_{n+1} , the ABAQUS software calls upon the UMAT subroutine to perform an integration of the behavior law. This access to the

subroutine is done for each of the numerical integration point elements. The schematic is based on the algorithms proposed by Simo et al. [32] for implementation of the Cap model. Since this is a multi-surface elastoplasticity model, there should be an intermediate algorithmic step between the elastic prediction and the plastic correction: that of the active plasticity mode detection.

The numerical integration of the behavior law is based on the integration of the flow rule according to an implicit Euler scheme, with time increment Δt between the instants t_n and t_{n+1} :

$$\Delta \epsilon^P = \sum_{i=1}^3 \Delta \lambda_i \frac{\partial f_i(\sigma, h)}{\partial \sigma} \tag{13}$$

where, $\Delta \lambda_i$ represents the plastic consistency parameter increment and $\Delta \epsilon^P$ designates the tensor of the plastic strain increment. This tensor is expressed as a function of the plastic deviatoric strain increment $\Delta \epsilon^P$ and the plastic volumetric strain increment tensor $\Delta \epsilon_v^P$:

$$\Delta \epsilon^P = \Delta \epsilon^P + \frac{1}{3} \Delta \epsilon_v^P \cdot \mathbf{1} \tag{14}$$

In a similar fashion, the total strain increment tensor $\Delta \epsilon$ is expressed as a function of the deviatoric strain increment and the volumetric strain increment. The same applies to the stress tensor σ that can be broken onto a deviatoric part \mathbf{s} and a spherical part I_1 :

$$\Delta \epsilon = \Delta \epsilon + \frac{1}{3} \Delta \epsilon_v \cdot \mathbf{1} \tag{15}$$

$$\sigma = \mathbf{s} + \frac{1}{3} I_1 \cdot \mathbf{1} \tag{16}$$

Furthermore, the tensor chosen to define the total strain increment $\Delta \epsilon$ can validly be decomposed additively into an elastic and a plastic part:

$$\Delta \epsilon = \Delta \epsilon^e + \Delta \epsilon^P \tag{17}$$

3.2.1 Elastic prediction

From a physical point of view, the elastic prediction consists of freezing the plastic yield and applying an elastic increment. This is basically to consider that, at instant t_{n+1} , the plastic strain is fixed and equal to the value at instant t_n . The stress obtained following this assumption, designated as the elastic predictor or the trial stress, is given by:

$$\begin{aligned} \sigma_{n+1}^{Trial} &= \mathbf{C} : (\epsilon_{n+1} - \epsilon_n^P) = \mathbf{C} : (\epsilon_n^e + \Delta \epsilon_{n+1}) \\ &= \sigma_n + \mathbf{C} : \Delta \epsilon_{n+1} \end{aligned} \tag{18}$$

Table 1 Algorithm for the finite element solver

Step 1	Set the iteration counter k to 0 Initialize the global Jacobian $[K^T]^0$ and the nodal displacement vector $\{u_{n+1}\}^0$ to their values at the configuration n Calculate the residual vector $\{\Delta R_{n+1}\}^0$
Step 2	Set $k=k+1$ Solve for $\{\Delta u_{n+1}\}^k$ the linearized problem: $[K^T]^{k-1} \{\Delta u_{n+1}\}^k = \{\Delta R_{n+1}\}^k$ Update the solution: $\{u_{n+1}\}^k = \{u_{n+1}\}^{k-1} + \{\Delta u_{n+1}\}^k$
Step 3	Check for convergence on both the displacement and the residual ◦If convergence, then set $n=n+1$ and go to next load increment ◦If no convergence, then: *For each element: *For each material integration point Compute the strain increment Retrieve the material point variables σ_n, κ_n and ρ_n Perform constitutive model integration using the closest point projection algorithm by calling the UMAT subroutine and obtain the values of $\sigma_{n+1}, \kappa_{n+1}$ and ρ_{n+1} in addition to the elastoplastic tangent moduli $H_{n+1}^{ep} = \frac{\partial \Delta \sigma}{\partial \Delta \epsilon}$ Store all the material point variables Compute and assemble the residual vector and the material stiffness matrix Go back to step 2 for another equilibrium iteration

Using the stress tensor decoupling principle (Eq. 16), the spherical and deviatoric components of the stress tensor are then obtained from the following equation:

$$\begin{aligned} I_{1,n+1}^{\text{Trial}} &= I_{1,n} + 3K \cdot \Delta\varepsilon_{v,n+1} \\ \mathbf{s}_{n+1}^{\text{Trial}} &= \mathbf{s}_n + 2G \cdot \Delta\mathbf{e}_{n+1} \end{aligned} \quad (19)$$

This last equation is used to predict if a plasticity state has been reached. Indeed, the yield function $f_{i,n+1}^{\text{Trial}}$ test values are obtained with this prediction. If all the test values for the $f_{i,n+1}^{\text{Trial}}$ functions are negative, then the load state was purely elastic. On the other hand, if some of the test functions become positive, the real stress state will be obtained after a plastic correction [33].

3.2.2 Plastic correction

The state of the material undergoing elastoplastic deformations is generally characterized by loading and unloading conditions. Thus, the plastic loading or the elastic loading/unloading is formulated according to the Kuhn-Tucker relations that govern the evolution of the plastic consistency parameters $\Delta\lambda_{i,n+1}$. These conditions, that must always be verified, stipulate that at each instant there must be:

$$\Delta\lambda_{i,n+1} \geq 0, f_{i,n+1} \leq 0 \quad \text{and} \quad f_{i,n+1} \cdot \Delta\lambda_{i,n+1} = 0, \quad i = 1, 2, 3. \quad (20)$$

This equation is used to characterize each of the Cap model's modes: elastic mode, tension mode, shear mode, cap mode, singular tension mode at $I_1 = T$, and singular compression mode at $I_1 = \kappa$ (Fig. 2).

Each mode will be identified in terms of limits to the elastically predicted stresses. Then, the plastic consistency parameters that allow calculation of the plastic strain are determined. The stress conditions of each one of the plastic modes is presented in Table 2, together with the corresponding values of the plastic consistency parameters increments. These values are then used to determine the plastic strain increment (Eq. 13) and thus, the real stress state (Eq. 19).

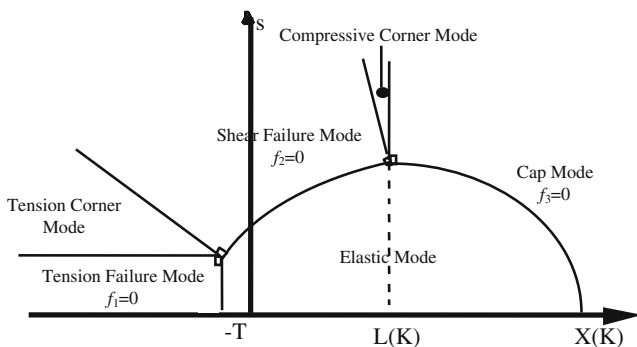


Fig. 2 Various elastoplastic modes within the Cap model

3.2.3 Elastoplastic tangent moduli

The last step in the numerical integration of the constitutive evolution equations is concerned with the determination of the powder medium's algorithmic material contribution to the FE tangent stiffness matrix. This contribution is computed at the integration point level and is called the elastoplastic tangent moduli. In order to preserve a quadratic rate of convergence for the global FE problem, this moduli should be derived from the algorithmic and not from the continuum mechanics formulation [33]. In fact, this material tangent moduli corresponds to the stress variation caused by an infinitesimal strain variation

$$\mathbf{H}^{ep} = \frac{d\sigma_{n+1}}{d\varepsilon_{n+1}} \quad (21)$$

It is therefore determined by a simple mathematical derivation of the relation between the actualized stresses and the strains:

$$d\sigma_{n+1} = \mathbf{C} : (d\varepsilon_{n+1} - d\varepsilon_{n+1}^p) \quad (22)$$

This formulation requires the determination of the plastic strain variation. The derivation of this module is performed differently if the active mode presents perfect plasticity or plasticity with hardening [33].

4 Inverse identification of the material parameters

Judicious use of the finite element simulation method rests on the precision and exactness of the behavior model used. To this end, it is not sufficient for the chosen model to be well adapted to the type of behavior being modeled but additionally, it is important to ensure that the model parameters represent the behavior of the material in question. Traditionally, the Cap model parameters are determined from a rheological analysis of experimental tests chosen for their suitability to the behavior being studied: resonant frequency, hydraulic compression, hydrostatic compression, triaxial compression, simple uniaxial compression, and special tests such as the Brazilian disk test [33–36]. In the identification process, the interpretation of the experimental trials usually requires the use of the homogenous deformation hypothesis in order to thresh out the results. However, the practical application of this hypothesis is a very difficult task for mechanical tests that are often not uniform and were aimed at characterizing the material. Furthermore, if the use of the Cap model for modeling the compression of ductile powders is fairly limited, it is mostly due to the difficulty in its parametrical and experimental characterization. Often, because of the hypotheses required by the experimental characterization

Table 2 Boundaries and plastic consistency parameters of the plastic modes

Failure mode	Stress state boundaries	Incremental consistency parameters
Tension	$\begin{cases} I_{1,n+1}^{\text{Trial}} \leq T \\ \ \mathbf{s}_{n+1}^{\text{Trial}}\ \leq F_s(T) \end{cases}$	$\begin{aligned} \Delta\lambda_{1,n+1} &= \frac{T - I_{1,n+1}^{\text{Trial}}}{9K} \\ \Delta\lambda_{2,n+1} &= 0 \\ \Delta\lambda_{3,n+1} &= 0 \end{aligned}$
Tension corner	$\begin{cases} I_{1,n+1}^{\text{Trial}} \leq T \\ F_s(T) < \ \mathbf{s}_{n+1}^{\text{Trial}}\ < F_s(T) + \frac{2G}{9K} \frac{T - I_{1,n+1}^{\text{Trial}}}{dF_s(T)/dI_1} \end{cases}$	$\begin{aligned} \Delta\lambda_{1,n+1} &= \frac{\ \mathbf{s}_{n+1}^{\text{Trial}}\ - F_s(T)}{2G}, \\ \Delta\lambda_{2,n+1} &= \frac{T - I_{1,n+1}^{\text{Trial}}}{9K} - \Delta\lambda_{1,n+1} \frac{dF_s(T)}{dI_1} \\ \Delta\lambda_{3,n+1} &= 0 \end{aligned}$
Shear	$\begin{cases} I_{1,n+1}^{\text{Trial}} \leq \kappa_n \\ F_s(T) + \frac{T - I_{1,n+1}^{\text{Trial}}}{dF_s(T)/dI_1} < \ \mathbf{s}_{n+1}^{\text{Trial}}\ \\ \ \mathbf{s}_{n+1}^{\text{Trial}}\ < F_s(\kappa_n) + \frac{\kappa_n - I_{1,n+1}^{\text{Trial}}}{dF_s(\kappa_n)/dI_1} \end{cases}$	$\begin{aligned} \Delta\lambda_{1,n+1} &= 0 \\ \Delta\lambda_{2,n+1} &= \frac{\ \mathbf{s}_{n+1}^{\text{Trial}}\ - F_s(I_{1,n+1})}{2G} \\ \Delta\lambda_{3,n+1} &= 0 \end{aligned}$
Compressive corner	$\begin{cases} I_{1,n+1}^{\text{Trial}} < \kappa_n \\ \ \mathbf{s}_{n+1}^{\text{Trial}}\ > F_s(\kappa_n) + \frac{2G}{9K} \frac{\kappa_n - I_{1,n+1}^{\text{Trial}}}{dF_s(\kappa_n)/dI_1} \end{cases}$	$\begin{aligned} \Delta\lambda_{1,n+1} &= 0 \\ \Delta\lambda_{2,n+1} &= \frac{\kappa_n - I_{1,n+1}^{\text{Trial}}}{9K dF_s(\kappa_n)/dI_1} \\ \Delta\lambda_{3,n+1} &= \frac{\ \mathbf{s}_{n+1}^{\text{Trial}}\ - F_s(\kappa_n)}{2G} - \Delta\lambda_{2,n+1} \end{aligned}$
Cap	$\begin{cases} L(\kappa_n) < I_{1,n+1}^{\text{Trial}} \leq X(\kappa_n) \\ \ \mathbf{s}_{n+1}^{\text{Trial}}\ > F_c(I_{1,n+1}^{\text{Trial}}) \end{cases} \quad \text{or} \quad I_{1,n+1}^{\text{Trial}} > X(\kappa_n)$	$\begin{aligned} \Delta\lambda_{1,n+1} &= 0 \\ \Delta\lambda_{2,n+1} &= 0 \\ \Delta\lambda_{3,n+1} &= \frac{R^2 \Delta \epsilon_{v,n+1}^p F_s(\kappa_{n+1})}{3(I_{1,n+1} - \kappa_{n+1})} \end{aligned}$

approach, the parameter sets available do not reproduce real practical situations. Thus, the identification of parameters using the inverse method directly from industrial production components represents an attractive alternative to the classical procedure since it emanates from practical situations and avoids the hypothesis of homogenous deformation altogether [37, 38].

4.1 Nonlinear optimization process

The optimization task is based on the Levenberg–Marquardt algorithm [39, 40] in order to determine the parameter corrections while the finite element solver handles the solution of the direct problem. The principal goal of this optimization process is to determine elasticity (E, G), failure surface ($\alpha, \beta, \gamma, \theta$), hardening law (W, D), and cap surface (r_1, r_2, r_3) parameters for the plasticity Cap model that are represented by the vector $\mathbf{p}=(E, G, T, \alpha, \beta, \gamma, \theta, W, D, r_1, r_2, r_3)$. However, a sensitivity study of the model showed that, when dealing with powder compaction with no excessive distortion, only the hardening law and cap surface parameters exert a preponderant influence on the final density prediction in the compact [41]. Thus, only the parameters describing the cap failure surface and the hardening law of the constitutive model are estimated by means of inverse modeling, the elastic parameters as well as the shear failure parameters are predetermined from an experimental material characteriza-

tion of the cap model [41]. Consequently, the parameter vector to be identified is reduced to $\mathbf{p}=(W, D, r_1, r_2, r_3)$.

Estimating these parameters involves adjusting the parameters in the finite element models until the calculated density vector ρ^{cal} coincides as the least square with the measured density vector ρ^{exp} . This is accomplished by minimizing the cost function Φ with respect to the vector of parameters \mathbf{p} :

$$\Phi(\mathbf{p}) = \frac{1}{2} \sum_{i=1}^m [\mathbf{r}_i(\mathbf{p})]^2 = \frac{1}{2} \mathbf{r}^T \mathbf{r} \tag{23}$$

where m is the number of measurements. The residual vector, \mathbf{r} , is defined by

$$\mathbf{r} = \rho^{\text{exp}} - \rho^{\text{cal}} \tag{24}$$

The minimization of Eq. 23 is subject to constraints on the parameters based on the physics of the problem. The constraints are written in the form:

$$c_j(\mathbf{p}) \geq 0 \quad j = 1, q \tag{25}$$

where c_j are the constraint functions and q is the number of constraints. The set of \mathbf{p} which satisfies the constraints is called the feasible region. In many problems, it is important to maintain the feasibility of the parameters throughout the solution process in order to carry out the finite element analyses. In the current estimation, bounds are required to prevent the parameters from becoming negative.

The parameter constraints, enforced by the interior penalty function method, are incorporated directly in the objective function, Φ^* , as follows:

$$\Phi^*(\mathbf{p}) = \Phi(\mathbf{p}) + \sum_{j=1}^q \zeta_j(\mathbf{p}) \quad (26)$$

where the weighted penalty functions, ζ_j , are the inverse barrier functions:

$$\zeta_j(\mathbf{p}) = \frac{\omega_j}{c_j(\mathbf{p})} \quad j = 1, q \quad (27)$$

with ω_j being the non-negative weights.

The nonlinear least squares problem is solved using a modified Levenberg–Marquardt method to account for the weighted penalty functions included in the objective function Φ^* . Starting from an initial feasible parameter guess, the modified Levenberg–Marquardt method determines a sequence of corrections to the parameters until convergence is achieved according to specified criteria. The convergence criterion for the optimization study is based on the variation of the objective function value. If differences in the objective function value between two subsequent iterations is less than a specified positive number ξ ,

$$\left\| \Phi^*(\mathbf{p}^{k+1}) - \Phi^*(\mathbf{p}^k) \right\| < \xi \quad (28)$$

the optimization process will stop and the final optimization is achieved. The parameter correction, $\delta\mathbf{p}^k$, at iteration k is calculated from the following system of equations:

$$\left(\mathbf{J}^{(k)T} \mathbf{J}^{(k)} + \mu^{(k)} \mathbf{I} + \mathbf{h}^{(k)} \right) \delta\mathbf{p}^{(k)} = -\mathbf{J}^{(k)T} \mathbf{r}^{(k)} + \mathbf{g}^{(k)} \quad (29)$$

where μ is Levenberg–Marquardt damping parameter (a non-negative scalar), \mathbf{J} is the Jacobian matrix of Φ , and \mathbf{g} and \mathbf{h} contain the first and the second order derivatives, respectively, of the weighted penalty functions with respect to the parameters. The elements of \mathbf{J} , \mathbf{g} , and \mathbf{h} are given by

$$J_{is} = \frac{\partial r_i}{\partial p_s} = \frac{\partial p_i^{\text{cal}}}{\partial p_s} \quad i = 1, m, \quad s = 1, n \quad (30)$$

$$g_s = -\sum_{j=1}^q \frac{\partial \zeta_j}{\partial p_s} \quad s = 1, n \quad (31)$$

$$h_{st} = -\sum_{j=1}^q \frac{\partial^2 \zeta_j}{\partial p_s \partial p_t} \quad s, t = 1, n \quad (32)$$

Recall that m is the number of measured data and n is the number of parameters.

To facilitate the choice of the Levenberg–Marquardt parameter μ and improve the conditioning of the

system, Eq. 29 is scaled before it is solved. Defining \mathbf{A} and \mathbf{b} as:

$$\mathbf{A} = \mathbf{J}^T \mathbf{J} + \mathbf{h} \quad (33)$$

$$\mathbf{b} = -\mathbf{J}^T \mathbf{r} + \mathbf{g} \quad (34)$$

The scaled matrix $\underline{\mathbf{A}}$ and the scaled vector $\underline{\mathbf{b}}$ are then defined as:

$$\underline{A}_{st} = \frac{A_{st}}{\sqrt{A_{ss}A_{tt}}} \quad s, t = 1, n \quad (35)$$

$$\underline{b}_s = \frac{b_s}{\sqrt{A_{ss}}} \quad s = 1, n \quad (36)$$

The scaled form of Eq. 29 to be solved for $\delta\mathbf{p}$ is then written as:

$$(\underline{\mathbf{A}} + \mu \mathbf{I}) \underline{\delta\mathbf{p}} = \underline{\mathbf{b}} \quad (37)$$

And $\delta\mathbf{p}$ is calculated from $\underline{\delta\mathbf{p}}$ using

$$\delta p_s = \frac{\delta p_s}{\sqrt{A_{ss}}} \quad s = 1, n \quad (38)$$

The fact that $\underline{A}_{ss} = 1$, $s = 1, n$, allows μ to be controlled in a manner that is problem independent and consistent from iteration to iteration.

Because the parameters are contained implicitly in the finite element formulation, a finite difference approximation of the Jacobian matrix \mathbf{J} in Eq. 29 is made. The Jacobian matrix is recalculated at every iteration by perturbing the parameters one at a time and solving a direct finite element problem for each perturbation.

The first derivatives of the penalty functions required to calculate \mathbf{g} are given by:

$$\frac{\partial \zeta_j}{\partial p_s} = -\frac{\omega_j}{c_j^2} \frac{\partial c_j}{\partial p_s} \quad j = 1, q, \quad s = 1, n \quad (39)$$

The second derivatives of the penalty functions required to calculate \mathbf{h} are approximated by

$$\frac{\partial^2 \zeta_j}{\partial p_s \partial p_t} \approx 2 \frac{\omega_j}{c_j^3} \left(\frac{\partial c_j}{\partial p_s} \right) \left(\frac{\partial c_j}{\partial p_t} \right) \quad j = 1, q, \quad s, t = 1, n \quad (40)$$

The modified Levenberg–Marquardt method and finite element analysis are integrated in the solution algorithm as shown in Table 3.

4.2 Application to the identification of the cap model parameters of iron powder

The method described above is applied to determine the cap material parameters of MP37HD iron powder

Table 3 Inverse finite element optimization algorithm

1. Initialize the parameters $\mathbf{p}^{(0)}$ and of the Levenberg-Marquardt damping parameter $\mu^{(0)}$
2. Solve the direct finite element problem at $\mathbf{p}^{(0)}$ and evaluate the cost function $\Phi^{(0)}$
3. Initialize the penalty functions weights ω_j . Evaluate the weighted penalty functions $\zeta_j^{(0)}$ and the objective function $\Phi^{*(0)}$
4. For iteration $k=0,1,2,\dots,K$
 - (a) Calculate the Jacobian matrix $\mathbf{J}^{(k)}$ using the finite differences method by solving n direct problems.
 - (b) Calculate the penalty function derivatives to form $\mathbf{h}^{(k)}$ and $\mathbf{g}^{(k)}$
 - (c) Solve Eq. 29 to determine the correction step to be applied to the parameters, $\delta\mathbf{p}^{(k)}$ and update the parameters $\mathbf{p}^{(k+1)} = \mathbf{p}^{(k)} + \delta\mathbf{p}^{(k)}$
 - (d) Solve the direct finite element problem at $\mathbf{p}^{(k+1)}$. Evaluate $\zeta_j^{(k+1)}$ and $\Phi^{*(k+1)}$
 - (e) Check if $\Phi^{*(k+1)} < \Phi^{*(k)}$
 - (1) If false, increase μ and return to step 4c $\mu^{(k)} = 10\mu^{(k)}$
 - (2) If true, reduce w_j and μ

$$\omega_j^{(k+1)} = 0.1\omega_j^{(k)}$$

$$\mu^{(k+1)} = 0.1\mu^{(k)}$$
 - (f) Verification that the convergence criteria is met
 - (1) If false, $k=k+1$ and return to step 4a
 - (2) If true, stop

manufactured by Domfer. The MP37HD powder grade used in this study was premixed with 0.375% Acrawax and 0.375% ST Lithium as lubricant and has a chemical composition by weight of Cu 1.80%, graphite 0.75%, and the balance is Fe. The industrial part, selected to apply the inverse identification approach to, is one whose geometry and filling positions for the different tools are given in Fig. 3. It is an axisymmetrical part with two levels. The tooling, used in the manufacturing of this part comprises a die, a core rod, an upper punch, and two lower punches.

The compaction sequence consists of four steps. The first two consist of the descent of upper punch 1 and lower punch 2. Lower punch 1 stays fixed throughout the entire process. During the third compaction phase, the die and core rod join the descent of the two punches. In the last step, only the die and the upper punch continue to descend. The compaction kinetics, described by the movement of the different tools (position in mm), is given in Table 4.

4.2.1 Finite element calculation of the answer

Considering both loading and geometric symmetries, an axisymmetric element needs to be used. Our preliminary analyses revealed that the eight-node CAX8 element has a problem with discontinuous equivalent plastic strain at its mid-node. Thus, we use the four node axisymmetric element and two degrees of freedom per node CAX4 which provides better numerical stability especially in the presence of high nonlinearities [42]. The lower degree of the CAX4 shape function is supplemented by placing fine elements at the critical regions of the part and by the fact that the initial mesh was oriented in the direction of compaction (Fig. 4).

The FE model consists of only about 456 elements and 591 nodes. We also place contact surfaces [42] at both the powder and tool surfaces of Fig. 4. In addition, since our main objective was the determination of the compact's density distribution, the simplest and numerically cheapest way to achieve this was to impose nodal displacements at

Fig. 3 Picture, geometry and tooling of the industrial part #1

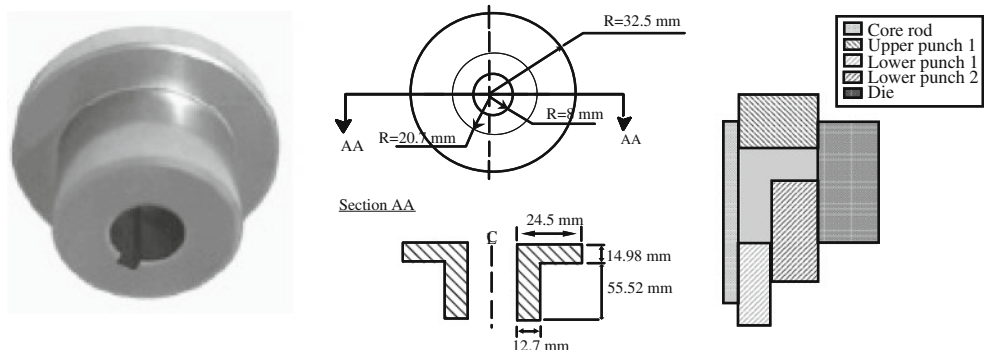


Table 4 Compression kinetics for industrial part #1

	Filling position	First step	Second step	Third step	Fourth step
Core rod	48	48	48	29.2	29.2
Die	48	48	48	29.2	22.6
Lower punch 1	-25.1	-25.1	-25.1	-25.1	-25.1
Lower punch 2	30.42	29.62	20.22	0	0
Upper punch 1	45.4	41.6	30.3	9.6	4.9

the powder boundary node sets. Also, as it can be seen in Fig. 4, large displacement contact with Coulomb friction was adopted for the interface regions between the powder cavity and tooling component sides. Moreover, since very small powder sliding occurs on punch faces, tied (sticking) contact was adopted for these interface regions. Both contact conditions were modeled using the “master-slave” contact pair formulation in ABAQUS [42]. This formulation requires the association of the master surface with the stiffer interacting body (tooling component) whereas the slave surface is associated with the second deformable body (powder cavity). The friction coefficient was assumed to be equal to 0.2 as in previous studies [43, 44] and its reliability was verified by comparing simulated results with experimental measurements as discussed in Section 5.

Moreover, the initial relative density of the powder is assumed to be uniformly spread and corresponds to a value of 36.5%. The applied load is translated into imposed motion on the surface of the tools according to Table 4. The tool motion is imposed in increments. For each increment of motion and for each element, the relative density of the powder at the integration points is calculated. Furthermore, in the finite element calculation, the multi-criteria Cap type constitutive model and the numerical integration schematic described above are used.

Furthermore, the four-step FE problem was solved by ABAQUS with a relatively small number of increments for

each one of the steps as indicated in Table 5. This table summarizes the number of global equilibrium and contact iterations required by the solver for each of the four load increments. It also shows the average local iterations needed at the integration point level by the implemented algorithm. It is clear that despite of the relatively large deformation increments, convergence of the closest point algorithm has required a relatively small number of iterations.

4.2.2 Parameters optimization

The optimization strategy consists of solving the direct problem using an initial set of the parameters, thus generating a calculated distribution of the final density of the compact, ρ^{cal} . To this numerical distribution, the experimental distribution ρ^{exp} , determined using the Vickers hardness method [45], is correlated. It is crucial that the initial guess of parameters is reasonable, e.g., parameters for a different powder mix. The optimization procedure has to struggle with many local minima which may appear far from physically acceptable values. It is normally necessary to start the optimization from different starting points to check the behavior in the neighborhood of the computed optimum. The initial parameter values were set close to the values obtained through the traditional experimental parameter estimation procedure for another type of powder, namely Distaloy AE [41].

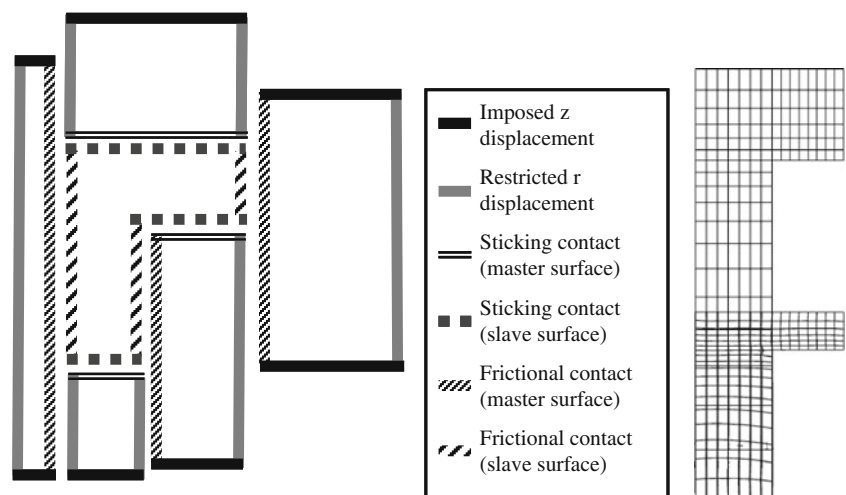
Fig. 4 Boundary conditions and initial and deformed mesh

Table 5 Summary of the numerical performance

Statistic	Step 1	Step2	Step 3	Step 4
Needed increments	17	18	18	18
Average number of global iterations per increment	9	9	13	13
Average number of local (UMAT) iterations per increment	12	10	13	14

The correspondence between the calculated density and the experimental density is hardly automatic. Indeed, the Vickers hardness measurement points are spread in a random manner on the part's surface and the meshing nodes, where the density is evaluated, do not coincide very often. Consequently, a smoothing technique had to be used in order to make the two measurement types' positions coincide. Three smoothing techniques were investigated: neural networks, kriging, and interpolation functions. The two first methods required processing that was external to the optimization module, thus offsetting the automatic aspect of the identification procedure. Furthermore, their application to this case seemed more complicated and required a higher calculation time. Thus, the interpolation functions that could be used on all the elements of the meshing, since they all possess the same reference element (quadrilateral element with 4 nodes), was deemed more suitable.

In the case under consideration here, the number of parameters to be identified is $n=5$. The number of measurements m , must therefore be greater than or equal to $n=5$. This condition is guaranteed to always be respected since the number of Vickers hardness measurements is generally quite high (in this case, $m=78$). Table 6 contains the identified parameter values for the iron powder whereas Figs. 5, 6, and 7 represent the evolution of the objective function and of different material parameters throughout the identification process.

5 An integrated software environment

In order to make the simulation of powder compaction an attractive design tool, an integrated simulation module has been developed. This module is mainly intended to facilitate and to automate some of the tedious modeling-

Table 6 Values of identified parameters for the iron powder

Parameter	Initial value	Identified value
W	0.8	0.864
D	0.1E-04	0.4091E-04
r_1	1.0	0.621
r_2	18.0	16.7
r_3	0.5	0.383

related tasks. It is composed of the I-Deas Master Series CAD software [46], the ABAQUS nonlinear FE solver [47], the ABAQUS-Post post-processing [48] software, an in-house developed pre-processing and interfacing program IDEQUS [49], and finally an inverse identification material parameters module INVMOD. The integrated software layout, as well as the main functions of its components, is described in Fig. 8.

5.1 Pre-processing

The pre-processing is first performed through I-Deas, in which the component geometries are defined and then meshed using a semi-automatic mapped pattern. User-defined macro functions, implemented into I-Deas, are then used for the selection and the identification of the special boundary regions of the powder cavity and tooling components. IDEQUS automatically identifies, generates, and pairs off contact surfaces using the element sets selected by the macro functions. All the information is written to a universal FE file which is then completed with additional information and then translated into the ABAQUS format by way of the IDEQUS program.

5.2 Processing

ABAQUS is an FE solver capable of handling both geometric and material nonlinearities, as well as the frictional contact nonlinearities. One of its main advantages is the open facility it offers for the definition of user material models. In fact, the cap material model was

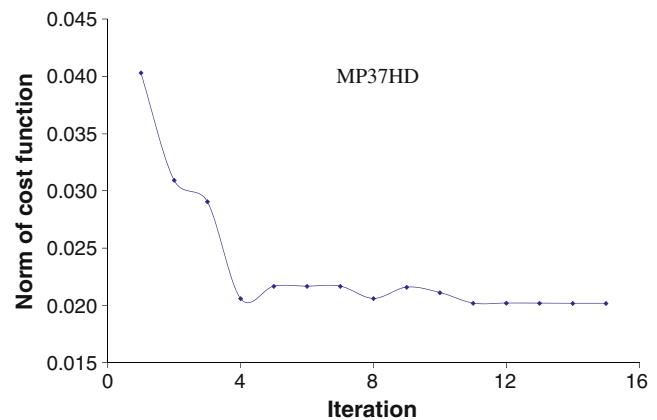


Fig. 5 Cost function evolution

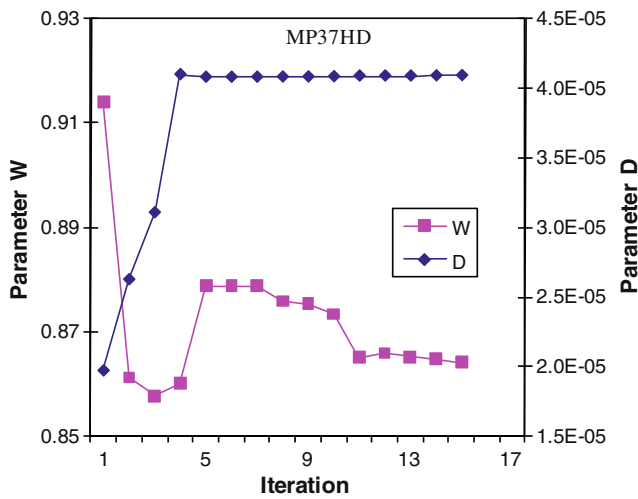


Fig. 6 Convergence of the hardening parameters

implemented into ABAQUS via the UMAT facility that allows the user to define a constitutive model and implement its numerical integration algorithm as a FORTRAN subroutine. Thus, UMAT is called by the main program at each element integration point within every equilibrium iteration of each load increment in the deformation process. The global FE problem was solved using the classical Newton–Raphson method with a line-search algorithm whereas the local material integration was handled by the closest point projection algorithm.

5.3 Post-processing

The ABAQUS-Post software is used mainly for the visualization of the predicted density maps within the compacts. The stress distribution, as well as the deformed shape of the tooling components, could also be post-processed by the same software.

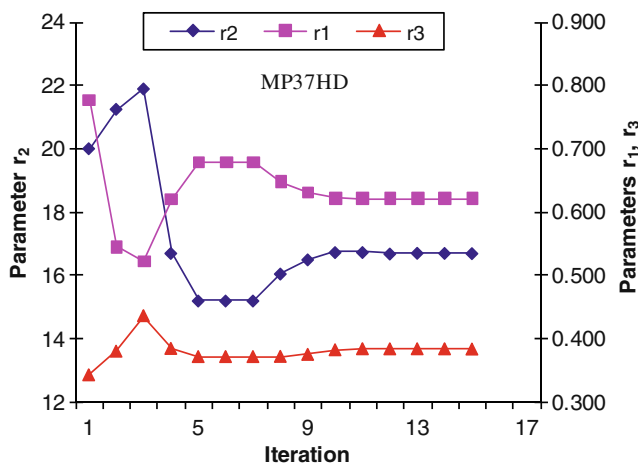


Fig. 7 Convergence of the coefficients with respect to the cap surface axes ratio

5.4 Inverse identification module

The main task of this module is to identify a selected set of unknown parameters of the numerical cap model. The unknown parameters are determined iteratively by minimizing a cost function which expresses the discrepancy between the experimental and the computed response of the physical system under study, e.g., by comparing density distributions. The experimental densities are determined by means of the Vickers hardness technique. The numerical density distributions are computed with the FE model. The a priori unknown material parameters in the FE model are iteratively updated in such a way that the computed densities match the measured densities as closely as possible. Figure 9 shows a flowchart of the applied inverse method.

6 Validation

6.1 Validation of the inverse results with classical tests

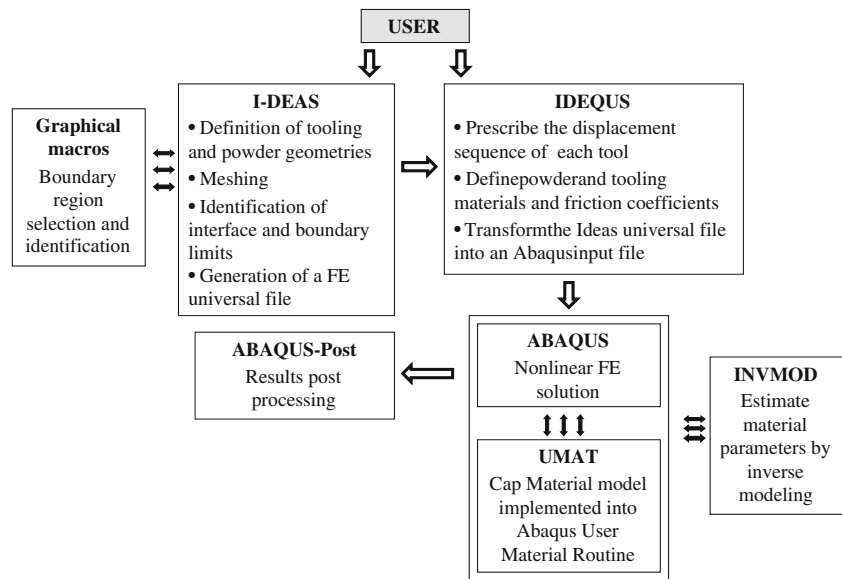
The Cap plasticity material parameters of the iron powder has been identified by Hrairi [41] based on the classical homogenous tests. The aspect ratio and the hardening parameters are determined by triaxial tests and isostatic compaction respectively. Data from the triaxial load paths as well as data points generated by the hydrostatic tests were used to draw the iso-density curves representing the cap surfaces at different relative densities. This fit shows an increasing aspect ratio R as a function of density that follows the empirical relation

$$R(\rho) = r_1(\rho - r_2)^{r_3} = 1.148(\rho - 38)^{0.208} \quad (41)$$

To determine the premix hardening law, we had to find the volumetric plastic strain ϵ_v^p as a function of I_1 , the hydrostatic component of stress. For every isostatically pressed specimen we determined ϵ_v^p using the initial loose density and the final measured post compaction density (Eq. 11). The obtained values were plotted against the first stress invariant corresponding to the hydrostatic pressures that served to produce the specimen. This fitting process (Eq. 9) permitted the determination of the hardening parameters $W=0.847$ and $D=0.4418E-04$. W being a measure of the maximum achievable volumetric plastic strain.

A sensitivity study of the model, based on simulations planned and analyzed using the Taguchi method, revealed that, when dealing with powder compaction with no excessive distortion, the most influential parameters on the final density distribution are those related to the hardening of the material. The identified values of the

Fig. 8 Integrated software framework for powder compaction simulation



different parameters are summarized in Table 7 as well as their respective relative influence on the final density distribution in a compact, as determined by the sensitivity analysis.

It can be noted from Table 7 that the results of the inverse method and the classic, homogeneous tests are quite similar when it comes to the hardening parameters but differ considerably for the aspect ratio parameters. This discrepancy can probably be explained by the fact of the almost no contribution of these parameters to the final density distribution in a compact. As one can see from

Table 7, the influence of $R(\rho)$ sums to 4.4% compared to a whopping 65.6% and 8% for W and D , respectively. Thus, the physical system under consideration, i.e., the measurement of final density, is rather insensitive to the values of $R(\rho)$. As a result it is hard to determine r_1 , r_2 , and r_3 as accurately as W and D . Therefore, in addition to the final density in the compact, more measurable responses should be taken into account in future research in order to accurately determine all the parameters of the Cap plasticity model.

6.2 Application of the results on an industrial part

The pressing of a gear, as shown in Fig. 10, is simulated to evaluate the estimated material parameters. Manufacture of this part requires, other than the core rod and die, two upper punches and three lower punches. Lower punch 1 does not move, lower punch 2 is mounted on a spring, and there is a level in upper punch 2.

The compaction sequence is made up of three steps. During the first step, lower punches 2 and 3, as well as the two upper punches, begin to descend. Lower punch 1 remains fixed throughout the process. During the second

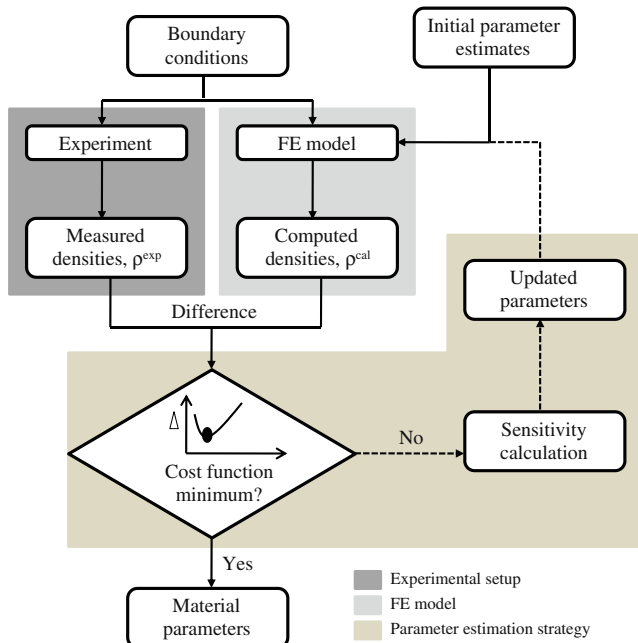


Fig. 9 Flow-chart of the inverse method for material parameters identification

Table 7 Values and relative importance of the iron powder parameters

Parameter	Inverse method	Classical tests	Contribution (%)
W	0.864	0.847	65.6
D	0.4091E-4	0.4418E-4	8.0
r_1	0.621	1.148	1.45
r_2	16.7	38	1.07
r_3	0.383	0.208	1.88

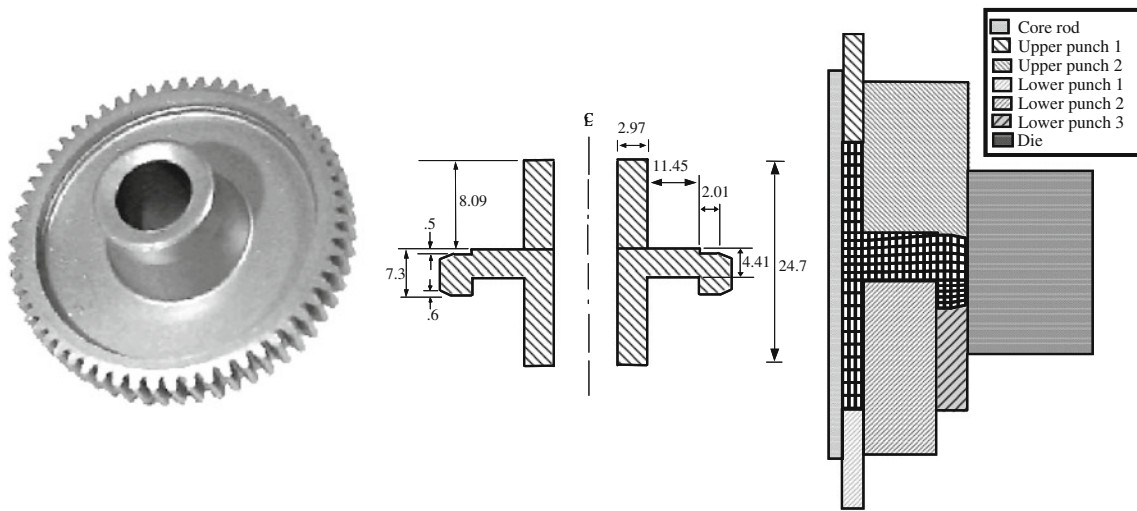


Fig. 10 Picture, geometry and tooling of industrial part #2

compaction step, the die and the core rod join the descent of the punches. At the end of this step, the two upper punches continue to descend, thus ensuring the compaction of the part from the top. The compaction kinetics, describing the motion of the various tools (position in mm), is given in Table 8.

Results from the simulations are depicted in Fig. 11 together with an experimentally measured density distribution using the Vickers hardness method. This method was applied on compacted parts according to the prescribed kinematics (Table 8) leading to the density distributions shown in Fig. 11b. This Vickers hardness measurement technique was used to obtain apparent hardness also called macrohardness, i.e., the average hardness of a porous material. Its procedure is well documented in ASTM E92-82 standard [50]. This standard offers various loading from 1–120 kgf applied to an indenter of pyramidal geometry with face angle of 136°. In this work, a 5 kgf load (HV 5) was used as recommended in MPIF standard 43 [51]7. Measurements were performed on five billets of different densities. Each billet had two faces on which $n=15$ hardness measurements were realized in a 3×5 pattern. Using a linear regression technique, the relative density of

green compacts and the logarithm of Vickers hardness can be correlated with a linear model:

$$\rho = 19.306 \log(\text{HV}) + 39.831 \quad (42)$$

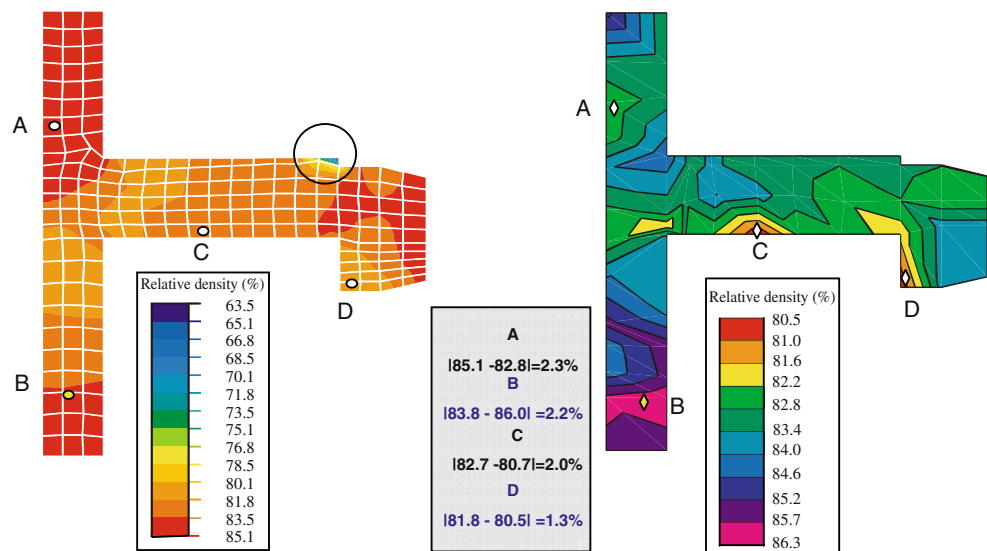
Error limits introduced by this model, by sample preparation factors and by the hardness measurements can be established to $\pm\sqrt{(0.05 + 7.8/n)}$ with a confidence level of 68%. Curiously, most of the error is caused by the Vickers measurement, and thus, can significantly be reduced by taking and averaging “n” measurements in a small area. The standard variation on Vickers hardness measurements was typically under 3 kg/mm². This results in an inaccuracy of approximately 2% in the worst cases, i.e., at low density ranges.

The computed density distribution, based on the estimated parameters, shows a reasonable agreement with the experimental result along the outer boundary and in the center. However, along the core rod, the computed results differ more compared to the experiment. As illustrated at some critical points in the compact, the maximum absolute error between densities was found to be 2.3% corresponding to the precision of the experimental method.

Table 8 Compression kinetics for industrial part #2

	Filling position	First step	Second step	Third step
Core rod	43.821	43.821	31.765	27.255
Die	43.821	43.821	31.765	20.005
Lower punch 1	-12.2	-12.2	-12.2	-12.2
Lower punch 2	14.68	11.716	0	0
Lower punch 3	8.819	7.877	-2.989	-2.989
Upper punch 1	43.595	36.385	24.355	12.5
Upper punch 2	24.613	17.403	5.373	4.411

Fig. 11 Final density distribution within the compact: **a** numerical, **b** experimental



However, one can notice a big discrepancy between the range of the relative density of simulation results which varies from 63.5% to 85.1% and that of the experimental data which shows a variation between 80.5% and 86.38%. This difference in range is seen only in the circled zone where there is a sharp change of section (Fig. 11). The numerical simulation rightly predicts this important density gradient (63.5–80.1%). However, no local density measurements could be achieved in this region of the part. In fact, this region was fractured during its metallographic preparation. This fracture was predictable from the simulation results that showed an important density gradient near this corner of the part. Consequently, a global density measuring technique was applied to the fractured region. The obtained value (72%) agrees well with simulated results, stating that in that region, density varies between 63.5% and 80.1%

Since the results obtained showed the desired degree of precision, the meshing initially proposed was deemed adequate and did not require further adjustment. The simulation of this compaction sequence without the necessity for an intermediate meshing would not have been possible if the initial meshing had not been conceived as a function of the kinetics used in the manufacturing of this part.

7 Conclusion

This work has been focused on a unified approach for parameters identification of P/M specimens in powder compaction process. Thus, it has created an integrated simulation environment capable of using finite elements and inverse optimization to evaluate the density distribution resulting from the compaction process. The problem of rigid die compaction of ductile metal powders involves

material, geometric as well as contact nonlinearities. While the last two nonlinearities were handled automatically by the ABAQUS FE solver, the first involves a material model unavailable in ABAQUS and hence the elastoplastic cap model had to be formulated and integrated into the software in order to be able to simulate the behavior of the metal powder medium. The closest point projection algorithm was used for the numerical integration of the multisurface plasticity model. Due to its flexibility and capacity to represent all the compaction stages, the cap material model was shown to yield very good results as far as the final density was the main concern and despite the fact that the model was not completely characterized. This is however expectable since the final density is mainly sensitive to the cap hardening parameters which seem to have been correctly identified.

Using this integrated simulation module, the simulation of the compaction of an industrial PM part has been performed successfully thus demonstrating the practical industrial applications of the computational approach. Indeed, a comparison between the experimental results and those obtained by simulation, using parameters identified inversely, revealed that the maximum absolute error between densities was found to be 2.3% corresponding to the precision of the experimental method. Also, the results from the current work show that inverse modeling of the powder-pressing experiment is a viable method for determining material parameters. It serves as an alternative to the already established methods and is generally less expensive to carry out. The concept proposed in this work is a flexible approach for identification of cap material model and can be useful to apply the results to metalworking industry. The information derived can be used for the subsequent quantitative design as well as optimization of the powder metallurgy processes.

In the current work, the parameters describing the cap failure surface and the hardening law of the constitutive model have been determined. To be able to determine the elastic moduli as a function of density and compacting pressure by means of inverse modeling, several unloading steps should be incorporated in the experiment. This was not done in the experiments carried out here, thus calls for further investigations. It may be desirable also to have a separate experiment for the shear failure part of the model. Another research orientation will be the development of a 3D simulation module, capable of modeling general non-axisymmetric applications.

Acknowledgements The authors would like to acknowledge the assistance of Lynn Mason in editing this manuscript.

References

- German RM (1994) Powder metallurgy science. Metal Powder Industries Federation, Princeton, NJ
- Gurson AL (1977) Continuum theory of ductile rupture by void nucleation and growth. Part I. Yield criteria and flow rules for porous ductile media. *Transactions of the ASME. J Eng Mat Technol* 99:2–15
- Shima S, Oyane M (1976) Plasticity theory for porous materials. *Int J Mech Sci* 18:285–291
- Gurson AL, McCabe J (1992) Experimental determination of yield functions for compaction of blended metal powder. *Adv Powder Metall Part Mater* 2:133–147
- Abou-Chedid G, Brown S (1992) On the mechanical behavior of metal powder compaction. *Adv Powder Metall Part Mater* 2:1–10
- Drucker D, Prager W (1952) Soil mechanics and plastic analysis on limit design. *Quart J Applied Math* 10:157–175
- Schofield AN, Wroth CP (1968) Critical state solid mechanics. McGraw Hill, New York
- DiMaggio, FL, Sandler, IS (1971) Material model for granular soils. *J Eng Mech Div* 97:935–950
- Sandler IS, Rubin D (1979) An algorithm and a modular subroutine for the Cap model. *Int J Numer Anal Methods Geomech* 3:173–186
- Falgon D, Vidal-Salle E, Boyer JC, Peczkalski R, Andrieu J (2005) Identification procedure of a hardening law for powder compaction. *Powder Technol* 157:183–190
- Michrafay A, Ringenbacher D, Tchoreloff P (2002) Modeling the compaction behavior of powders: application to pharmaceutical powders. *Powder Technol* 127:257–266
- Cunningham JC, Sinka IC, Zavaliangos A (2004) Analysis of tablet compaction. I. Characterization of mechanical behavior of powder and powder/tooling friction. *J Pharm Sci* 93:2022–2039
- Wu CY, Ruddy OM, Bentham AC, Hancock BC, Best SM, Elliott JA (2005) Modeling the mechanical behavior of pharmaceutical powders during compaction. *Powder Technol* 152:107–117
- Wu CY, Hancock BC, Mills A, Bentham AC, Best SM, Elliott JA (2008) Numerical and experimental investigation of capping mechanisms during pharmaceutical tablet compaction. *Powder Technol* 181:121–129
- Frenning G (2007) Analysis of pharmaceutical powder compaction using multiplicative hyperelasto-plastic theory. *Powder Technol* 172:102–112
- Gurson AL, Postoraro RA (1992) Yield functions for metal powders for use in the numerical simulation of powder compaction. TMS Conference, San Diego, CA
- Chtourou H, Gakwaya A, Guillot M (2002) Modeling of the metal powder compaction process using the cap model. Part II: numerical implementation and practical applications. *Int J Solids Struct* 39:1077–1096
- Erhart T, Wall WA, Ramm E (2005) A robust computational approach for dry powders under quasi-static and transient impact loadings. *Comput Meth Appl Mech Eng* 194:4115–4134
- Rossi R, Alves MK, Al-Qureshi HA (2007) A model for the simulation of powder compaction processes. *J Mater Process Technol* 182:286–296
- Khoei AR, Azami AR, Azizi S (2007) Computational modeling of 3D powder compaction processes. *J Mater Process Technol* 185:166–172
- Lee SC, Kim KT (2007) A study on the Cap model for metal and ceramic powder under cold compaction. *Mater Sci Eng, A* 445–446:163–169
- Szantoa M, Bierb W, Fragec N, Hartmann S, Yosibash Z (2008) Experimental based finite element simulation of cold isostatic pressing of metal powders. *Int J Mech Sci* 50:405–421
- Pizette P, Martin CL, Delette G, Sornay P, Sans F (2010) Compaction of aggregated ceramic powders: from contact laws to fracture and yield surfaces. *Powder Technol* 198:240–250
- Andersson DC, Larsson PL, Cadario A, Lindskog P (2010) On the influence from punch geometry on the stress distribution at powder compaction. *Powder Tech* 202(1–3):78–88
- Peric D (1992) On consistent stress rates in solid mechanics: computational implications. *Int J Numer Methods Eng* 33:799–817
- Peric D, Owen DRJ, Honnor ME (1992) A model for finite strain elasto-plasticity based on logarithmic strains: computational issues. *Comput Meth Appl Mech Eng* 94:35–61
- Chtourou H, Gakwaya A, Guillot M, Hrairi M (1995) Implementing a cap material model for the simulation of metal powder compaction. *Net Shape Processing of Powder Materials*, AMD-vol. 216, ASME, San Francisco, CA, pp. 19–27
- Alm O (1983) Mechanical testing of powders and powder compacts. *Scand J Metall* 12:302–311
- Weber GG, Brown SB (1989) Simulation of the compaction of powder components. *Adv Powder Metall Part Mater* 1:105–118
- Simo JC, Ortiz M (1985) A unified approach to finite deformation elastoplasticity based on the use of hyperelastic constitutive equations. *Comput Meth Appl Mech Eng* 49:222–245
- Simo JC, Taylor RL (1986) A return mapping algorithm for plane stress elastoplasticity. *Int J Numer Methods Eng* 22:649–670
- Simo JC, Ju JW, Pister KS, Taylor RL (1988) Assessment of Cap model: consistent return algorithms and rate-dependent extension. *J Eng Mech* 114:191–218
- Hofstetter G, Simo JC, Taylor RL (1993) A modified Cap model: closest point solution algorithms. *Comput Struct* 46(2):203–214
- Chtourou H, Gakwaya A, Guillot M (2002) Modeling of the metal powder compaction process using the cap model. Part I: experimental material characterization and validation. *Int J Solids Struct* 39:1059–1075
- Pavier E, Doremus P (1996) Mechanical behaviour of a lubricated iron powder. In: Cadle TM, Narasimhan KS (eds) *Advances in powder metallurgy and particulate materials—1996*. Metal Powder Industries Federation, USA, pp 6–40
- Mosbah P (1995) Modeling and experimental study of metal powders behaviour during comaction in closed die. Ph.D. thesis, University Joseph Fourier-Grenoble I, Grenoble, France
- Gelin JC, Ghouati O (1995) An inverse method for material parameters estimation in the inelastic range. *Comput Mech* 16(3):143–150
- Mahnken R, Stein E (1996) A unified approach for parameter identification of inelastic material models in the frame of the finite element method. *Comput Meth Appl Mech Eng* 136:225–258

39. Levenberg K (1944) A method for the solution of certain nonlinear problems in least squares. *Quart Appl Math* 2:164–168
40. Marquardt DW (1963) An algorithm for least squares estimation of nonlinear parameters. *SIAM J Appl Math* 11:431–441
41. Hrairi M (1999) *Modélisation Numérique et Identification Directe et Inverse du Comportement des Poudres Métalliques lors du Procédé du Compactage*. Ph.D. Thesis, Laval University, Québec
42. Abaqus (1995) *Theory Manual Version 5.5*. Hibbit, Karlsson and Sorenson, Inc., Rhode Island
43. Samuelson P, Bolin B (1983) Experimental studies of frictional behavior of hard metal powders sliding on cemented carbide walls. *Scand J Metall* 12:315–322
44. Khoei AR, Biabanaki SOR, Vafa AR, Taheri-Mousavi SM (2009) A new computational algorithm for 3D contact modeling of large plastic deformation in powder forming processes. *Comput Mater Sci* 46:203–220
45. Guillot M, Chtourou H (1996) Generalization of the Vickers hardness local density measurement technique to different powder materials. *Proceedings of the World Congress on Powder Metallurgy and Particulate Materials*, vol. 1, part 4, pp.31–40
46. SDRC Corporation (1994) *Ideas Master Series Student Guide*
47. Hibbitt K (1997) *ABAQUS theory manual, Version 5.7*, Sorensen, Inc., Boston, USA
48. Hibbitt K (1997) *ABAQUS-post user guide, Version 5.7*, Sorensen, Inc., Boston, USA
49. Chtourou H, Gakwaya A, Guillot M, Hrairi M (1996) Finite element simulation of the rigid die compaction of metal powder components. *Proceedings of the Canadian Society of Mechanical Engineers Forum*. McMaster University, Hamilton, Canada
50. ASTM E92-82 (1987) *Standard test method for Vickers hardness of metallic materials*
51. MPIF Standard 43 (1991). *Method for determination of hardness of powder metallurgy products*, Princeton, NJ